Eleventh International Conference on Computational Fluid Dynamics (ICCFD11), Maui, Hawaii, July 11-15, 2022

ICCFD11-2022-2105

A Polydisperse Gaussian-Moment Method for Extended Statistical Modelling of Multiphase Flows

M. Marchildon*, B. Allard*, L. Ivan**, J.G. McDonald*,**
Corresponding author: James.McDonald@uottawa.ca

* University of Ottawa, Ottawa, ON, Canada, K1N 6N5.
** Canadian Nuclear Laboratories, Chalk River, ON, Canada, K0J 1J0.

Abstract: A novel model is proposed for the Eulerian treatment of particle-laden multiphase flows characterized by a dilute particle phase with an arbitrary number of distinguishable properties, such as size or temperature, based on an entropy-maximization argument. Unlike previous formulations, this new moment-based model provides a set of first-order robustly-hyperbolic balance laws that include a direct treatment for the local statistical variance of each variable, as well as the covariance between the internal variables or the internal variables and particle velocity. Two variations of the model are investigated and the predictive capabilities of the new model are explored for two representative problems. First, the ability of one version of the model to exactly capture the state of a polydisperse particle phase settling in still air is shown. Then, a puff of particles with initial horizontal velocity is modelled settling in a cross wind in order to demonstrate the value of directly tracking all particle variances and covariances for accurate prediction.

1 Introduction and Scope of Work

The accurate prediction of multiphase flow when particles are differentiated by a set of distinguishable properties, such as size or temperature, can pose modelling and numerical challenges. Even for monodisperse flow, traditional Eulerian methods have modelling limitations. Most of these models only treat a small number of variables describing the particle phase—typically the density and velocity [1, 2]. As most of these classical models assume that all particles at a location in space share the same velocity, they are inappropriate for situations when a range of particle velocities is expected. More recently, models for monodisperse flows that are inspired by the kinetic theory of gases have been proposed [3, 4, 5, 6, 7]. These model allow for the direct treatment of higher-order statistics of particle velocities, such as variances and co-variances.

The focus of this work is the exploration of two different formulations of a recently proposed polydisperse Gaussian-moment model (PGM). These models, building upon the recent PGM formulation of Forgues *et al.* [8], are described by fifteen first-order hyperbolic balance laws that provide an Eulerian treatment for higher-order statistics describing a particle phase in a background flow. The PGM formulation is an extension of the well-known ten-moment maximum-entropy model from rarefied gas dynamics [9, 10] and provides a direct treatment for local variances and covariances between all particle properties and velocities. This statistical information is not commonly available or utilized in traditional Eulerian methods and holds the promise of improved modelling accuracy at reduced computational cost.

Two variants of the PGM are investigated: the original form, which assumes a log-normal distribution of particle diameters, and one in which particle surface area is assumed to follow a normal distribution. In both cases, particle drag, buoyancy, and gravitational acceleration are considered. There are many practical processes in which a log-normal distribution of the particle diameters is encountered such as the human cough [11]. However, the original log-normal version of the model does not correctly recover the settling rates for particles in a quiescent atmosphere. In contrast, the surface-area-based version of the model is designed to recover this settling rate exactly.

2 Moment Methods and the Kinetic Theory of Gases

The situation of a mutliphase flow, in which a large number of small particles are suspended in a background fluid, has many similarities to the situation of an ideal gas. Such flows contains a large number of particles but their individual evolution are rarely of interest. Rather, it is the evolution of the bulk that is important. The theory of moment methods from the kinetic theory of gases provides a framework for the construction of evolution laws for observable statistics of the collection of particles [12]. This chapter summarizes the essential elements of the kinetic theory of gases and the construction of the maximum-entropy family of moment closures. These closures form the basis of the moment-based models for polydisperse flows that are proposed in the following section.

2.1 An Introduction to Kinetic Theory of Gases

In a traditional kinetic-theory model, a gas is assumed to be comprised of discrete, indistinguishable particles. These particles are treated in a statistical manner, such that, for a given position in phase space (position, x_i, and velocity, v_i), the density of particles at a given time, t, is given by a distribution function, $\mathcal{F} = (x_i, v_i, t)$. The evolution of this distribution function is governed by the Boltzmann equation,

$$\frac{\partial \mathcal{F}}{\partial t} + v_\alpha \frac{\partial \mathcal{F}}{\partial x_\alpha} + \frac{\partial}{\partial v_\alpha}\left(a_\alpha \mathcal{F}\right) = \frac{\delta \mathcal{F}}{\delta t}\,. \tag{1}$$

Here, a_α is the particle acceleration induced by external fields and the right-hand side is the Boltzmann collision integral [13]. This integral models the effect that inter-particle collisions have on the distribution function.

The distribution function is a high-dimensional function that provides an enormous amount of information describing the state of a gas—far more than is usually of interest. Traditional macroscopic, or observable, properties of the gas are obtained by taking moments of $\mathcal{F}$. This is done by pre-multiplying the distribution by a suitably chosen velocity-dependant weight and integrating over all velocity space,

$$\iiint_{-\infty}^{\infty} w\,\mathcal{F}(x_i, v_i, t)\,\mathrm{d}v_i = \langle\, w\,\mathcal{F}\,\rangle\,. \tag{2}$$

Here, w is a velocity dependant weight (typically a monomial). The compact notation, $\langle\cdot\rangle$, indicates integration over all possible velocities. The lowest-order moment, the local number density of a gas, can be obtained by choosing $w = 1$,

$$n(x_i, t) = \iiint_{-\infty}^{\infty} \mathcal{F}(x_i, v_i, t)\,\mathrm{d}v_i\,. \tag{3}$$

As the particle velocity appears zero times in the weight, this is denoted as a zeroth-order moment. Another zeroth-order moment, the mass density, is found by taking $w = m$, where m is the mass of an individual gas particle,

$$\rho = \langle\, m\,\mathcal{F}\,\rangle\,. \tag{4}$$

Taking the first-order moment, $w = mv_i$, results in the corresponding average momentum density of the particles,

$$\rho\mu_i = \langle\, mv_i\,\mathcal{F}\,\rangle\,. \tag{5}$$

The average particle velocity of the distribution can thus be obtained as

$$\mu_i = \frac{\langle\, mv_i\,\mathcal{F}\,\rangle}{\langle\, m\,\mathcal{F}\,\rangle}\,, \tag{6}$$

Additionally, it becomes useful to defined the random, or deviatoric, velocity of the particles as the difference between the particle's velocity, and the local average velocity of the gas, $c_i = v_i - \mu_i$.

The deviatoric velocity can also be used to define velocity moments. For example, the moment

$$n\Theta_{ij} = \langle c_i c_j \mathcal{F} \rangle \ . \tag{7}$$

defines the second-order variance-covariance tensor, Θ_{ij}. This symmetric tensor contains the variance of each component of the particle velocity on the diagonal and covariance between components off the diagonal. It is related to the so-called pressure tensor as

$$P_{ij} = \rho\Theta_{ij}. \tag{8}$$

This pressure tensor is the negative of the traditional fluid stress tensor and is related to the hydrostatic pressure through the contraction, $p = P_{ii}$.

2.2 Moments Methods

Due to its high dimensionality, the direct numerical solution of Eq. (1) is prohibitively costly for practical cases. It would be unfeasible to solve this kinetic equation, then take moments in most cases. Fortunately, the method of moments provides a technique to produce evolution laws for the moments themselves. This process begins by taking moments of the Boltzmann equations,

$$\left\langle w \left(\frac{\partial \mathcal{F}}{\partial t} + v_\alpha \frac{\partial \mathcal{F}}{\partial x_\alpha} + \frac{\partial}{\partial v_\alpha} \left(a_\alpha \mathcal{F} \right) \right) \right\rangle = \left\langle w \frac{\delta F}{\delta t} \right\rangle \ , \tag{9}$$

$$\left\langle w \frac{\partial \mathcal{F}}{\partial t} \right\rangle + \left\langle w v_\alpha \frac{\partial \mathcal{F}}{\partial x_\alpha} \right\rangle + \left\langle w \frac{\partial}{\partial v_\alpha} \left(a_\alpha \mathcal{F} \right) \right\rangle = \left\langle w \frac{\delta F}{\delta t} \right\rangle \ , \tag{10}$$

$$\frac{\partial}{\partial t} \langle w \mathcal{F} \rangle + \frac{\partial}{\partial x_\alpha} \langle v_\alpha w \mathcal{F} \rangle + \left\langle w \frac{\partial}{\partial v_\alpha} \left(a_\alpha \mathcal{F} \right) \right\rangle = \left\langle w \frac{\delta F}{\delta t} \right\rangle \ . \tag{11}$$

This equation is known as Maxwell's equation of change and describes the evolution of the moment, $\langle w\mathcal{F} \rangle$. The last term on the left-hand side, caused by external acceleration fields, can be converted to another form that is often more convenient by using the product rule,

$$\left\langle \frac{\partial}{\partial v_\alpha} \left(a_\alpha w \mathcal{F} \right) \right\rangle = \left\langle w \frac{\partial}{\partial v_\alpha} \left(a_\alpha \mathcal{F} \right) \right\rangle + \left\langle a_\alpha \mathcal{F} \frac{\partial w}{\partial v_\alpha} \right\rangle \ . \tag{12}$$

Provided that $\mathcal{F}$ goes to zero quickly enough as $v_i \to \infty$, the left-hand side of Eq. (12) will be zero.

Typically, one is interested in the evolution of more than one moment. One can, therefore, define a vector of weights, $\boldsymbol{\mathcal{W}}$, containing a collection of generating weights. This leads to

$$\frac{\partial}{\partial t} \langle \boldsymbol{\mathcal{W}} \mathcal{F} \rangle + \frac{\partial}{\partial x_\alpha} \langle v_\alpha \boldsymbol{\mathcal{W}} \mathcal{F} \rangle = \left\langle \boldsymbol{\mathcal{W}} \frac{\delta F}{\delta t} \right\rangle + \left\langle a_\alpha \mathcal{F} \frac{\partial \boldsymbol{\mathcal{W}}}{\partial v_\alpha} \right\rangle \ . \tag{13}$$

Both moments on the right-hand side of this equation typically lead to local, algebraic expressions. Equation (13), therefore, takes the form of a system of first-order balance laws,

$$\frac{\partial}{\partial t} \boldsymbol{U} + \frac{\partial}{\partial x_\alpha} \boldsymbol{F_\alpha} = \boldsymbol{S} \, . \tag{14}$$

Here $\boldsymbol{U} = \langle \boldsymbol{\mathcal{W}} \mathcal{F} \rangle$ is the solution vector containing the moments of interest and $\boldsymbol{F_\alpha} = \langle v_\alpha \boldsymbol{\mathcal{W}} \mathcal{F} \rangle$ is the flux dyad corresponding to the conserved moment in $\boldsymbol{U}$. If the eigenvalues of the flux Jacobian of this system contains all real eigenvalues, the system is said to by hyperbolic—a property that brings mathematical and computational benefits.

One can observe that Eq. (13) or (14) are not closed. This is because all moments present in the solution vector, $\boldsymbol{U}$, always depend on knowledge of a higher-order moment in the flux term, $\boldsymbol{F_\alpha}$. This means there will always be moments present in the flux that are not present in the solution vector. In general, the source terms can also be unclosed. However, for many practical cases, this is not the case. A technique to close the system of balance laws given in Eq. (14) is known as a moment closure.

2.3 Moment Closure

One technique to obtain a closed system of balance laws describing the evolution of the moments of interest is to restrict the form of the distribution function, $\mathcal{F}$. If one wishes to close a system of n moment equations, a form for $\mathcal{F}$ is proposed in terms of n free parameters, or closure coefficients. The values of the coefficients should be chosen so that moment relations, such as those given in Eqs. (3)–(7), are satisfied. Once this is done, the distribution function is completely determined and any missing moments can be integrated.

The method of moments for gases was first proposed by Grad [12], who proposed to select a distribution function that is an expansion around thermodynamic equilibrium in terms of polynomials. Unfortunately, it was quickly discovered that the resulting moment systems led to first-order balance laws whose flux Jacobian could develop complex eigenvalues. Also, the polynomial expansion is not guaranteed to remain positive and, thus, the assumed distribution function can be negative in some regions of phase space. These facts have limited the wide-spread adoption of the method.

More recently, a hierarchy of moment methods based on the maximization of entropy was proposed [14, 15, 9]. The hierarchy comes from assuming the distribution function has the form

$$\mathcal{F} = \exp\left(\boldsymbol{\alpha}^{\boldsymbol{T}}\boldsymbol{\mathcal{W}}\right). \tag{15}$$

Here, $\boldsymbol{\alpha}$ is the vector of closure coefficients that must be found to ensure the distribution function is consistent with the moments of the solution vector.

This hierarchy appears to have many pleasing properties. The resulting moment equations are guaranteed to be hyperbolic whenever a function of the form given in Eq. (15) can be found and the positivity of the distribution is guaranteed by the assumed form of the distribution.

The lowest-order member of the maximum-entropy hierarchy is obtained by choosing a vector of generating weights, $\boldsymbol{\mathcal{W}}_5 = [m, mv_i, \frac{1}{2}mv_iv_i]^{\mathrm{T}}$. This gives an assumed form of the distribution function given by

$$\mathcal{F}_5 = n\left(\frac{\rho}{2\pi p}\right)^{\frac{3}{2}} \exp\left(-\frac{\rho}{2p}c_ic_i\right), \tag{16}$$

which is the Maxwell-Boltzmann distribution that describes a gas in local thermodynamic equilibrium, and leads to the familiar Euler equations for a compressible monatomic gas.

The next member of the maximum-entropy family of closures uses the ten moments that correspond to velocity weights, $\boldsymbol{\mathcal{W}}_{10} = [m, mv_i, mv_iv_j]^{\mathrm{T}}$. This leads to a distribution function given by

$$\mathcal{F}_{10} = \mathcal{G} = \frac{n}{(2\pi)^{\frac{3}{2}}\left(\det\Theta_{ij}\right)^{\frac{1}{2}}} \exp\left(-\frac{1}{2}\Theta_{ij}^{-1}c_ic_j\right). \tag{17}$$

This so-called Gaussian distribution resembles the Maxwell-Boltzmann distribution, but has a different variance in different directions. In the absence of acceleration fields, it leads to a collection of ten first-order hyperbolic balance laws,

$$\frac{\partial\rho}{\partial t} + \frac{\partial}{\partial x_k}\rho\mu_k = 0, \tag{18}$$

$$\frac{\partial}{\partial t}\rho\mu_i + \frac{\partial}{\partial x_k}\left(\rho\mu_i\mu_k + P_{ik}\right) = 0, \tag{19}$$

$$\frac{\partial}{\partial t}\left(\rho\mu_i\mu_k + P_{ik}\right) + \frac{\partial}{\partial x_k}\left(\rho\mu_i\mu_j\mu_k + \mu_iP_{jk} + \mu_jP_{ik} + \mu_kP_{ij}\right) = \Delta(P_{ij}). \tag{20}$$

Here, $\Delta(P_{ij})$ describes how inter-particle collisions attenuate anisotropy in the pressure tensor. This term depends of the particular collision operator chosen. This closure provides a first-order hyperbolic treatment for viscous compressible gases. It obtains its closure because the heat transfer is zero through the choice of the distribution function. However, this model has been used to successfully model many viscous flows in situations when heat-transfer can be neglected [10, 16, 17, 18, 19, 20, 21]. This model has also previously been applied to the prediction of monodisperse flows with good results [3]. It is this Gaussian model that forms the basis of the treatments for polydisperse multiphase proposed in the present work.

3 A Kinetic Description of Polydisperse Flow

The goal of this work is to extend the moment methods presented in the previous section for the treatment of polydisperse multiphase flows. The situation of a particle phase is similar to that of the particles comprising a gas, which gives confidence that similar moment-based technique should be effective. Previous studies have shown this to be true for a monodisperse flow, in which the particles are indistinguishable [3]. However, the particles of a general polydisperse flow can be differentiated by any number of distinguishing variables, such as size, temperature, or chemical composition. In order to treat such flows, the traditional distribution function must be extended into higher dimensions,

$$\mathcal{F} = \mathcal{F}(x_i, v_i, \zeta_{\breve{i}}, t)\,. \tag{21}$$

Here, the $\zeta_{\breve{i}}$ can be replaced by any number of distinguishing variables describing particles and $\mathcal{F}$ gives the particle density in this expanded phase space. The index decorated with a breve, $\breve{i}$, indexes the distinguishing variables, which do not transform as regular tensors—undecorated indices are reserved for traditional spacial components of tensors.

The evolution of the extended distribution function is described by the expanded kinetic equation,

$$\frac{\partial \mathcal{F}}{\partial t} + v_\alpha \frac{\partial \mathcal{F}}{\partial x_\alpha} + \frac{\partial}{\partial v_\alpha}\left(a_\alpha \mathcal{F}\right) + \sum_{\breve{i}=0} \frac{\partial}{\partial \zeta_{\breve{i}}}\left(\Upsilon_{\breve{i}} \mathcal{F}\right) = \left(\frac{\delta \mathcal{F}}{\delta t}\right)_{\text{collision}}\,. \tag{22}$$

Here, $\Upsilon_{\breve{i}}$ represents the time rate of change of the $\breve{i}$th distinguishing variable.

Moments of the extended distribution function are once again defined. However, the integration must now be expanded into the space of distinguishing variables,

$$\langle w\mathcal{F}\rangle = \underset{\infty}{\iiint\cdots\int} w\mathcal{F}\,\mathrm{d}\zeta_{\breve{i}}\,\mathrm{d}v_i\,. \tag{23}$$

It should be noted that the space of these new variables need not span all real numbers. For example, if the particle surface area, s, is chosen, this distinguishing variable can only take values in the half space, $0 < s < \infty$.

In addition to the moments defined above, the distinguishing variables can also be used as moment weights. For example, the average value of a distinguishing variable, $\bar{\zeta}_{\breve{i}}$, can be found as

$$n\bar{\zeta}_{\breve{i}} = \langle \zeta_{\breve{i}}\,\mathcal{F}\rangle\,. \tag{24}$$

This allows the deviatoric velocity, c_i, to be extended with deviations of other variables from the average,

$$c_{\tilde{i}} = \left[v_x - \mu_x,\ v_y - \mu_y,\ v_z - \mu_z,\ \zeta_0 - \bar{\zeta}_0,\ \zeta_1 - \bar{\zeta}_1,\ \zeta_2 - \bar{\zeta}_2,\ \ldots\right]^{\mathrm{T}}\,, \tag{25}$$

where indices decorated with a tilde, $c_{\tilde{i}}$, indicate an expanded index comprising the traditional spacial directions and added distinguishing variables[1]. This allows an expanded variance-covariance tensor to be defined as

$$n\Psi_{\tilde{i}\tilde{j}} = n\begin{bmatrix} \Theta_{ij} & \Psi_{i\breve{j}} \\ \Psi_{j\breve{i}} & \Psi_{\breve{i}\breve{j}} \end{bmatrix} = \left\langle c_{\tilde{i}} c_{\tilde{j}} \mathcal{F}\right\rangle\,. \tag{26}$$

The off-diagonal entries, $\Psi_{i\breve{j}}$, contain the covariances between components of the particle velocity and particular distinguishing variables, while $\Psi_{\breve{i}\breve{j}}$ contains variances and covariances between the distinguishing variables themselves.

One again, moments of the kinetic equation, Eq. (22), can be taken. This leads to an extended Maxwell's equation of change,

$$\frac{\partial}{\partial t}\langle w\mathcal{F}\rangle + \frac{\partial}{\partial x_\alpha}\langle v_\alpha w\mathcal{F}\rangle = \left\langle w\frac{\delta \mathcal{F}}{\delta t}\right\rangle + \left\langle a_\alpha \mathcal{F}\frac{\partial w}{\partial v_\alpha}\right\rangle + \sum_{\breve{i}=0}\left\langle \Upsilon_{\breve{i}}\mathcal{F}\frac{\partial w}{\partial \zeta_{\breve{i}}}\right\rangle - \sum_{\breve{i}=0}\left\langle \frac{\partial}{\partial \zeta_{\breve{i}}}\left(w\Upsilon_{\breve{i}}\mathcal{F}\right)\right\rangle\,. \tag{27}$$

[1] It should be noted that the Einstein summation convention is also applied to indices decorated with tildes.

One should note that, unlike in Eq. (12), the last term on the right-hand side of Eq. (27) is not necessarily zero, if the domain of one or more of the distinguishing variables is not $(-\infty, \infty)$.

4 The Polydisperse Gaussian Model

As in the classical case, for general distribution functions, Eq. (27) is not closed. One must choose an assumed form. In the present work, the Gaussian distribution function, shown in Eq.(28), is extended to the expanded phase space as

$$\mathcal{G} = \exp\left(-\frac{1}{2}M^{-1}_{\tilde{i}\tilde{j}}\hat{c}_{\tilde{i}}\hat{c}_{\tilde{j}} + k\right), \tag{28}$$

where $M_{\tilde{i}\tilde{j}}$ and k are closure coefficients, while $\hat{c}_{\tilde{i}}$ is the deviation of the position in the expanded phase space from the peak of the Gaussian distribution. When substituted into the expanded Maxwell's equation of change, Eq. (27), this leads to a set of first-order balance laws, known as the polydisperse Gaussian model (PGM),

$$\frac{\partial n}{\partial t} + \frac{\partial}{\partial x_k}\, n u_k = S^{(1)}, \tag{29}$$

$$\frac{\partial}{\partial t}\, n u_i + \frac{\partial}{\partial x_k}\, n(u_i u_k + \Theta_{ik}) = S^{(2)}_i, \tag{30}$$

$$\frac{\partial}{\partial t}\, n\left(u_i u_j + \Theta_{ij}\right) + \frac{\partial}{\partial x_k}\, n\left(u_i u_j u_k + u_i\Theta_{jk} + u_j\Theta_{ik} + u_k\Theta_{ij} + Q_{ijk}\right) = S^{(3)}_{ij}, \tag{31}$$

$$\frac{\partial}{\partial t}(n\zeta_{\check{i}}) + \frac{\partial}{\partial x_k}\, n\left(u_k\zeta_{\check{i}} + \Psi_{k\check{i}}\right) = S^{(4)}_{\check{i}}, \tag{32}$$

$$\frac{\partial}{\partial t} n(u_i\zeta_{\check{j}} + \Psi_{i\check{j}}) + \frac{\partial}{\partial x_k}\, n\left(u_i u_k\zeta_{\check{j}} + u_i\Psi_{k\check{j}} + u_k\Psi_{i\check{j}} + \zeta_{\check{j}}\Theta_{ik} + Q_{i\check{j}k}\right) = S^{(5)}_{i\check{j}}, \tag{33}$$

$$\frac{\partial}{\partial t}\, n(\zeta_{\check{i}}\zeta_{\check{j}} + \Psi_{\check{i}\check{j}}) + \frac{\partial}{\partial x_k}\, n\left(u_k\zeta_{\check{i}}\zeta_{\check{j}} + \zeta_{\check{i}}\Psi_{k\check{j}} + \zeta_{\check{j}}\Psi_{k\check{i}} + u_k\Psi_{\check{i}\check{j}} + Q_{\check{i}\check{j}k}\right) = S^{(6)}_{\check{i}\check{j}}. \tag{34}$$

Here, $Q_{\tilde{i}\tilde{j}k} = n\langle c_{\tilde{i}}c_{\tilde{j}}c_k\mathcal{F}\rangle$ is related to the skewness of the distribution function. By the assumed form of the distribution function, it will be equal to zero if the domain of all distinguishing variables spans all real numbers, but can be non-zero if any of the distinguishing variables have smaller domains.

In these six equations, the terms on the right-hand side, $S^{(1)}$ to $S^{(6)}_{\check{i}\check{j}}$, result from the integrals on the right-hand side of Eq (27). These terms will be local expressions whenever the particle acceleration, a_i, and the rate of change of each internal variable, $\Upsilon_{\check{i}}$, are local. The exact form of these terms depends entirely on the effects experienced by the particles and which internal variables are treated.

4.1 Two Polydisperse Gaussian Models

In this work, two specializations of the PGM in terms of a single distinguishing variable are considered. Each model describes a polydisperse flow in which particles are distinguished by size. In the original model, the logarithm of the particle diameter is chosen as the distinguishing variable. This leads to an assumed form of the distribution of particle diameters that is log-normal. A second PGM is also considered in which the distinguishing variable is chosen as the particle surface area. This new PGM has been proposed as it is able to recover the exact settling rate of particles subjected to Stokes drag. This was not the case for the original PGM, which predicted that particles would settle at a slightly incorrect rate. However, the fact that the values for which the particle surface area is defined is only the half space, $[0, \infty)$, leads to more complicated moment equations.

For both models, simple particle-acceleration models are chosen. Particles are assumed to experience gravity, buoyancy, and Stokes drag. This leads to a particle acceleration given by

$$a_i = \frac{V_i - v_i}{\tau} + \phi_i, \tag{35}$$

with

$$\phi_i = \frac{\rho_p - \rho_f}{\rho_p} g_i \,. \tag{36}$$

In these expressions, V_i is the local value of the background velocity, ρ_p is the density of the material making up the particles, ρ_f is the density of the background fluid, and g_i is the gravitational acceleration. The time scale associated with Stokes drag is given by

$$\tau = \frac{\rho_p \, d^2}{18 \mu_f} = \gamma s \,, \tag{37}$$

where d is the particle diameter, μ_f is the viscosity of the background fluid, s is the particle surface area and $\gamma = \rho_p/(18\pi\mu_f)$ is a group defined for convenience, as it appears frequently in expressions related to the particle-drag source terms.

As the flows of interest in this work are disperse, inter-particle collisions are neglected. Thus, the collision operator is not treated in this work.

4.2 The original log-normal PGM

For the originally proposed PGM model, the logarithm of particle diameter is chosen as the sole distinguishing variable. This choice leads to a very nice model described by simple, closed-form balance laws with $Q_{\tilde{\tilde{ijk}}} = 0$, clean known wave speeds, and a simple entropy [8]. The resulting right-hand side for the moment equations, $\boldsymbol{S}$, is given by

$$\begin{bmatrix} 0 \\ \frac{n}{\tau_{\mathcal{G}}} \left(V_i - (u_i - 2\Psi_{id}) \right) + n\phi_i \\ \frac{n}{\tau_{\mathcal{G}}} \left(V_i (u_j - 2\Psi_{jd}) + V_j (u_i - 2\Psi_{id}) - 2(u_i u_j - 2u_i \Psi_{jd} - 2u_j \Psi_{id} + 4\Psi_{id}\Psi_{jd} + \Theta_{ij}) \right) + n \left(u_j \phi_i + u_i \phi_j \right) \\ 0 \\ \frac{n}{\tau_{\mathcal{G}}} \Big(V_i \left(\bar{\zeta}_d - 2\Psi_{dd} \right) - (\bar{\zeta}_d u_i - 2\bar{\zeta}_d \Psi_{id} - 2u_i \Psi_{dd} + 4\Psi_{dd}\Psi_{id} + \Psi_{id}) \Big) + n\bar{\zeta}_d \phi_i \\ 0 \end{bmatrix} . \tag{38}$$

In these expressions,

$$\tau_{\mathcal{G}} = \frac{\rho_p}{18 \mu f} e^{(2\bar{\zeta}_d - 2\Psi_{dd})} \tag{39}$$

and the "d" subscript is used to denote moments related to the logarithm of the particle diameter.

For a space-homogeneous situation of particles settling in a quiescent background, the moments of the original PGM reach a steady, terminal state described by

$$u_i = \phi_i \tau_{\mathcal{G}} (1 + 4\Psi_{dd}) \,, \tag{40}$$

$$\Theta_{ij} = 4\phi_i \phi_j \tau_{\mathcal{G}}^2 \Psi_{dd} \,, \tag{41}$$

$$\Psi_{id} = 2\phi_i \tau_{\mathcal{G}} \Psi_{dd} \,. \tag{42}$$

However, without the moment approximation imposed by the assumed distribution function, a collection of particles with a log-normal distribution of diameters would actually reach a terminal steady state of

$$\mu_i = \phi_i \, \tau_{\mathcal{G}} \, e^{4\Psi_{dd}} \,, \tag{43}$$

$$\Theta_{ij} = \phi_i \phi_j \, {\tau_{\mathcal{G}}}^2 \, e^{8\Psi_{dd}} \left(e^{4\Psi_{dd}} - 1 \right) \,, \tag{44}$$

$$\Psi_{id} = 2\phi_i \, \tau_{\mathcal{G}} \, \Psi_{dd} e^{4\Psi_{dd}} \,. \tag{45}$$

Through a Taylor-series expansion, one case see that, for small values of Ψ_{dd}, the correct solution agrees with the moment approximation. However, as this variance increases, deviations grow. It is the inability of the original PGM to correctly predict the particle settling rate that motivated the development of the new closure based on the particle surface area.

4.3 A New Particle-Surface-Based PGM

It is thought that correctly predicting the terminal settling rate of particles is important for a range of applications, including the accurate prediction of atmospheric dispersion or the modelling of biological aerosols generated by coughs or sneezes. The terminal velocity of a spherical particle subjected to Stokes drag is well known to be

$$v_i = \frac{1}{18}\frac{(\rho_p - \rho_f)}{\mu_f} g_i d^2 = \gamma \phi_i s \,. \tag{46}$$

That is, the particle settling velocity is proportional to the surface area of the particle. If a PGM model is to recover this behaviour exactly, one of the primary stress axes of the distribution function must be along a line in velocity-surface area space. This is only possible if the particle surface area is chosen as the distinguishing variable that characterizes the particle size. The domain of this variable is the positive half space, $0 \leq s \leq \infty$.

The restricted domain of allowable particle surface areas (non-negative), leads to more complicated expressions for the moment equations. Defining the closure coefficients of Eq. (28) to be

$$M_{\tilde{i}\tilde{j}} = \begin{bmatrix} p_{ij} & q_{is} \\ q_{js} & r_{ss} \end{bmatrix} \quad \text{with} \quad \hat{c}_{\tilde{i}} = \begin{bmatrix} v_i - \hat{u}_i \\ s - \hat{s} \end{bmatrix} , \tag{47}$$

their values can be found through expressions given in Table 1a. In these expressions, the "s" subscript denotes moments and coefficients related to the particle surface area and σ is the local mean surface area. The variable, $\mathcal{H}$, is the hazard rate. It is given by

$$\mathcal{H}(\chi) = \frac{\sqrt{\frac{2}{\pi}} \exp\left[-\frac{1}{2}\chi^2\right]}{1 + \operatorname{erf}\left(\frac{1}{\sqrt{2}}\chi\right)} \quad \text{with} \quad \chi = \frac{\hat{s}}{\sqrt{r_{ss}}} \,. \tag{48}$$

One of the advantages of using surface-weighted moments become apparent when evaluating the source term of the PGM. As the acceleration of the particles is directly affected by the inverse of the particles surface, Eq. (35) using surface-weighted statistics greatly simplifies the evaluation of the source term. For instance, evaluation of the first source term using surface-weighted statistics admits known and previously evaluated moments of the distribution. Whereas using non-weighted statistics would require knowledge of the following moment $\left\langle s^{-1}\mathcal{F}\right\rangle$. This choice has for added benefit that larger particles can be regarded as more important than the smaller particles. The moments defined above treat particles of every size as equally important in the moments. Once can, however, use weighted moments to give more influence to the larger particles. In this work, for the surface-area-based closure, all moments are weighted by the particle surface area. For example, the number density is replaced by the surface density as

$$\dot{n} = \langle s\mathcal{F}\rangle \ . \tag{49}$$

Other important moments are defined as

$$\dot{n}\dot{\mu}_i = \langle s v_i \mathcal{F}\rangle \ , \quad \dot{n}\dot{\sigma} = \left\langle s^2\mathcal{F}\right\rangle \ , \quad \dot{n}\dot{\Phi}_{\tilde{i}\tilde{j}} = \left\langle s c_{\tilde{i}} c_{\tilde{j}} \mathcal{F}\right\rangle \ , \quad \dot{n}\dot{Q}_{\tilde{i}\tilde{j}\tilde{k}} = \left\langle s c_{\tilde{i}} c_{\tilde{j}} c_{\tilde{k}} \mathcal{F}\right\rangle \ . \tag{50}$$

For these moments, the same symbols from the classical moments are maintained and decorated with dots. A new deviatoric vector is defined as $\dot{c}_{\tilde{i}} = [v_i - \dot{\mu}_i, s - \dot{\sigma}]^{\mathrm{T}}$. The relations between these moments and the closure coefficients are given in Tabel 1b.

As the particle surface area can only take on positive values, the expanded phase space is truncated in this variable. This leads to a skewness of the distribution function, as it is not defined for negative particle surface areas. The third-order deviatoric moment, needed in the PGM moment equations, can be computed for both traditional and sufrace-area weighted moments. The expressions are given in Table 1c.

For the remainder of this work, surface-weighted statistics are used for the surface-area-based variant of

Table 1: Relationships between moments and closure coefficients for surface-area-based PGM

(a) Moments of the surface-based PGM

Name	Weight	Moment	Expression
Number Density	1	n	$2\pi^2 \det(M_{\tilde{i}\tilde{j}})^{\frac{1}{2}} e^k \left(1 + \mathrm{erf}\left(\frac{\hat{s}}{\sqrt{2r_{ss}}}\right)\right)$
Average Velocity	$\frac{v_i}{n}$	μ_i	$\hat{u}_i + \frac{q_{is}}{\sqrt{r_{ss}}}\mathcal{H}$
Average Surface	$\frac{s}{n}$	σ	$\hat{s} + \sqrt{r_{ss}}\mathcal{H}$
Velocity (Co)Variance	$\frac{1}{n}c_i c_j$	Θ_{ij}	$p_{ij} - q_{is}q_{js}\frac{\mathcal{H}}{r_{ss}^{3/2}}\sigma$
Velocity-Surface Covariance	$\frac{1}{n}c_i c_s$	Ψ_{is}	$q_{is} - q_{is}\frac{\mathcal{H}}{\sqrt{r_{ss}}}\sigma$
Surface Variance	$\frac{1}{n}c_s^2$	Ψ_{ss}	$r_{ss} - \sqrt{r_{ss}}\mathcal{H}\sigma$

(b) Surface-weighted (S-W) moments of the surface-based PGM

Name	Weight	Moment	Expression
Surface Density	s	$\dot{n}$	$n\sigma$
S-W Average Velocity	$\frac{sv_i}{\dot{n}}$	$\dot{\mu}_i$	$\hat{u} + \frac{q_{is}}{\sigma}$
S-W Average Surface	$\frac{s^2}{\dot{n}}$	$\dot{\sigma}$	$\hat{s} + \frac{r_{ss}}{\sigma}$
S-W Velocity (Co)Variance	$\frac{s}{\dot{n}}\dot{c}_i\dot{c}_j$	$\dot{\Psi}_{ij}$	$p_{ij} + \frac{q_{is}q_{js}}{\sigma^2}\left(\frac{\mathcal{H}}{\sqrt{r_{ss}}}\sigma - 1\right)$
S-W Velocity-Surgace Covariance	$\frac{s}{\dot{n}}\dot{c}_i\dot{c}_s$	$\dot{\Psi}_{is}$	$q_{is} + \frac{q_{is}r_{ss}}{\sigma^2}\left(\frac{\mathcal{H}}{\sqrt{r_{ss}}}\sigma - 1\right)$
S-W Surface Variance	$\frac{s}{\dot{n}}\dot{c}_s^2$	$\dot{\Psi}_{ss}$	$r_{ss} + \frac{r_{ss}^2}{\sigma^2}\left(\frac{\mathcal{H}}{\sqrt{r_{ss}}}\sigma - 1\right)$

(c) Skewness Moments

Weight	Moment	Closure Coefficients
$\frac{1}{n}c_i c_j c_k$	Q_{ijk}	$q_{is}q_{js}q_{ks}\frac{\mathcal{H}}{r_{ss}^{5/2}}\left(\left(2\mathcal{H}^2 - 1\right)r_{ss} + 3\hat{s}\sqrt{r_{ss}}\mathcal{H} + \hat{s}^2\right)$
$\frac{s}{\dot{n}}\dot{c}_i\dot{c}_j\dot{c}_k$	$\dot{Q}_{ijk}$	$\frac{q_{is}q_{js}q_{ks}}{\sigma}\left(\frac{2}{\sigma^2} - \frac{3\mathcal{H}}{\sqrt{r_{ss}}\sigma} - \frac{\hat{s}}{r_{ss}^{3/2}}\mathcal{H}\right)$
$\frac{1}{n}c_i c_j c_s$	Q_{ijs}	$q_{is}q_{js}r_{ss}\frac{\mathcal{H}}{r_{ss}^{5/2}}\left(\left(2\mathcal{H}^2 - 1\right)r_{ss} + 3\hat{s}\sqrt{r_{ss}}\mathcal{H} + \hat{s}^2\right)$
$\frac{s}{\dot{n}}\dot{c}_i\dot{c}_j\dot{c}_s$	$\dot{Q}_{ijs}$	$\frac{q_{is}q_{js}r_{ss}}{\sigma}\left(\frac{2}{\sigma^2} - \frac{3\mathcal{H}}{\sqrt{r_{ss}}\sigma} - \frac{\hat{s}}{r_{ss}^{3/2}}\mathcal{H}\right)$
$\frac{1}{n}c_i c_s^2$	Q_{iss}	$q_{is}r_{ss}^2\frac{\mathcal{H}}{r_{ss}^{5/2}}\left(\left(2\mathcal{H}^2 - 1\right)r_{ss} + 3\hat{s}\sqrt{r_{ss}}\mathcal{H} + \hat{s}^2\right)$
$\frac{s}{\dot{n}}\dot{c}_i\dot{c}_s^2$	$\dot{Q}_{iss}$	$\frac{q_{is}r_{ss}^2}{\sigma}\left(\frac{2}{\sigma^2} - \frac{3\mathcal{H}}{\sqrt{r_{ss}}\sigma} - \frac{\hat{s}}{r_{ss}^{3/2}}\mathcal{H}\right)$

the PGM. In this case, the resulting source terms for the moment equations are

$$\dot{\boldsymbol{S}} = \begin{bmatrix} 0 \\ \frac{n}{\gamma}\left(V_i - \mu_i\right) + \dot{n}\phi_i \\ \frac{n}{\gamma}\left(V_i\mu_j + V_j\mu_i - 2\left(\Psi_{ij} + \mu_i\mu_j\right)\right) + \dot{n}\left(\phi_i\mu_j + \phi_j\mu_i\right) \\ 0 \\ \frac{\dot{n}}{\gamma}\left(V_i - \dot{\mu}_i\right) + \dot{n}\dot{\sigma}\phi_i \\ 0 \end{bmatrix} . \tag{51}$$

One should note that these expressions contain both surface-weighted and regular moments. This is done because it greatly simplifies the form of the expressions.

One of the main motivations for investigating the surface-area-based PGM was in the hope of recovering particle settling exactly. For a still background, the above source term leads to a steady-state terminal state given by

$$\dot{\mu}_i = \phi_i\gamma\dot{\sigma} \,, \tag{52}$$

$$\dot{\Psi}_{ij} = \phi_i\phi_j\gamma^2\dot{\Psi}_{ss} \,, \tag{53}$$

$$\dot{\Psi}_{is} = \phi_i\gamma\dot{\Psi}_{ss} \,. \tag{54}$$

These are in perfect agreement with the exact solution of the kinetic equation with a distribution function for particles that have normally distributed surface areas. This agreement between the surface-based PGM and the kinetic equation for settling particles is further demonstrated in Section 6.

5 Robust Hyperbolicity of the PGM

Each variant of the PGM leads to a set of fifteen first-order balance laws that are robustly hyperbolic. This is true when either traditional or surface-weighted moments are used. This hyperbolicity is demonstrated here for the surface-weighted variant. The corresponding proof for the traditional moments is nearly identical and obvious once this form is understood.

The proof of hyperbolicity starts by remembering the general form of the distribution function, given in Eq. (15), and defining density and flux potentials,

$$h = \langle s\,\mathcal{F}\rangle \,, \quad \text{and} \quad j_i = \langle sv_i\mathcal{F}\rangle \,. \tag{55}$$

The solution vector and flux are the gradients of these potentials,

$$\boldsymbol{U} = \frac{\partial h}{\partial \boldsymbol{\alpha}} = \langle s\boldsymbol{\mathcal{W}}\mathcal{F}\rangle \,, \quad \text{and} \quad \boldsymbol{F}_i = \frac{\partial j_i}{\partial \boldsymbol{\alpha}} = \langle sv_i\boldsymbol{\mathcal{W}}\mathcal{F}\rangle \,. \tag{56}$$

One can also compute the Hessians

$$\frac{\partial \boldsymbol{U}}{\partial \boldsymbol{\alpha}} = \frac{\partial^2 h}{\partial \boldsymbol{\alpha}\partial \boldsymbol{\alpha}} = \left\langle s\boldsymbol{\mathcal{W}}\boldsymbol{\mathcal{W}}^{\mathrm{T}}\mathcal{F}\right\rangle \,, \quad \text{and} \quad \frac{\partial \boldsymbol{F}_i}{\partial \boldsymbol{\alpha}} = \frac{\partial^2 j_i}{\partial \boldsymbol{\alpha}\partial \boldsymbol{\alpha}} = \left\langle sv_i\boldsymbol{\mathcal{W}}\boldsymbol{\mathcal{W}}^{\mathrm{T}}\mathcal{F}\right\rangle \,. \tag{57}$$

This means the balance laws describing the system can be written as

$$\frac{\partial \boldsymbol{U}}{\partial t} + \frac{\partial \boldsymbol{F}_i}{\partial x_i} = \boldsymbol{S} \,, \tag{58}$$

$$\frac{\partial \boldsymbol{U}}{\partial \boldsymbol{\alpha}}\frac{\partial \boldsymbol{\alpha}}{\partial t} + \frac{\partial \boldsymbol{F}_i}{\partial \boldsymbol{\alpha}}\frac{\partial \boldsymbol{\alpha}}{\partial x_i} = \boldsymbol{S} \,, \tag{59}$$

$$\frac{\partial^2 h}{\partial \boldsymbol{\alpha}\partial \boldsymbol{\alpha}}\frac{\partial \boldsymbol{\alpha}}{\partial t} + \frac{\partial^2 j_i}{\partial \boldsymbol{\alpha}\partial \boldsymbol{\alpha}}\frac{\partial \boldsymbol{\alpha}}{\partial x_i} = \boldsymbol{S} \,. \tag{60}$$

The hyperbolicity of these equations is assured, as the two Hessians are symmetric, with the Hessian of the

Table 2: Initial conditions for space-homogeneous particle-settling case

(a) Surface-weighted moments

Moment	Initial value
$\dot{n}$	1
$\dot{\mu}_i$	$10\,\mathrm{m/s}$
$\dot{\Theta}_{ij}$	$(1\,\mathrm{m^2/s^2})\delta_{ij}$
$\dot{\sigma}$	$5.6\times10^{-7}\,\mathrm{m^2}$
$\dot{\Psi}_{is}$	$0\,\mathrm{m^3/s}$
$\dot{\Psi}_{ss}$	$8.58\times10^{-14}\,\mathrm{m^4}$

(b) Traditional moments

Moment	Initial value
n	1
μ_i	$10\,\mathrm{m/s}$
Θ_{ij}	$(1\,\mathrm{m^2/s^2})\delta_{ij}$
$\bar{\zeta}$	-8.11
Ψ_{id}	$0\,\mathrm{m/s}$
Ψ_{dd}	0.113

density potential also being positive definite, as

$$\boldsymbol{w}^{\mathrm{T}}\left\langle s\boldsymbol{\mathcal{W}}\boldsymbol{\mathcal{W}}^{\mathrm{T}}\mathcal{F}\right\rangle\boldsymbol{w}=\left\langle s\boldsymbol{w}^{\mathrm{T}}\boldsymbol{\mathcal{W}}\boldsymbol{\mathcal{W}}^{\mathrm{T}}\boldsymbol{w}\mathcal{F}\right\rangle=\left\langle s\left(\boldsymbol{w}^{\mathrm{T}}\boldsymbol{\mathcal{W}}\right)^2\mathcal{F}\right\rangle\geq 0 \tag{61}$$

for any non-zero vector, $\boldsymbol{w}$. The exact same proof can be done for the traditional PGM, but without the surface weighting in the density or flux potentials.

6 Numerical Results

In order to validate and compare the two presented version of the PGM, two test cases are considered. The first test case consists of a space-homogeneous distribution of particles with an initial downward velocity and variance of all properties. The particles come to a steady terminal state in which the effects of gravitational acceleration, buoyancy, and Stokes drag are balanced. Comparisons are made with solutions obtained through the direct numerical integration of the kinetic equation, Eq. (22), the solution of which is affordable in this case without spacial variations.

The second test case is a spherical puff of particles with initial horizontal velocity ejected into a transverse background flow. This case demonstrates the evolution of the higher-order statistics directly treated by the model and demonstrates how the inclusion of this information in the model leads to improved predictive capabilities.

6.1 Space-Homogeneous Particle Settling

The first numerical result is for a case in which the particle phase has no variation in any spacial direction. That is, all spacial derivatives in Eqs. (29)–(34) are zero. The system then degenerates into a coupled set of ordinary differential equations (ODEs) where the moment state evolves purely due to the source term. For this case, the initial conditions are chosen to be described by a surface-area-based distribution function with moments given in Table 2a. A cloud of particles has an initial downward (positive x in this case) velocity that is far higher than the terminal velocity. The particle cloud therefore decelerates to it's steady state settling configuration. The particles are modelled as being droplets of water in the medium of air such that the density of the particles and of the background are given by $\rho_p = 1000\,\mathrm{kg/m^3}$, and $\rho_f = 1.225\,\mathrm{kg/m^3}$, respectively. The dynamic viscosity of air is set as $\mu_f = 1.82\times10^{-5}\,\mathrm{m^2/s}$, which corresponds to ambient air at 20 °C. This leads to source-term parameters, $\gamma = 971\,641\,\mathrm{s/m^2}$ and $\phi_z = 9.79\,\mathrm{m/s^2}$, for a simplified expressions in the source term.

Both the surface-weighted PGM and the original log-normal PGM are investigated. In order to set initial conditions for the log-normal variant of the model, classical moments based on the logarithm of particle diameter must be evaluated for the initial condition. The values obtained are shown in Table 2b. These serve as the initial conditions for the log-normal PGM computation.

The ODEs are advanced in time until a steady-state for each model is obtained. This can be seen as the terminal-velocity state of each model. Results are shown in Figure 1. Comparisons between each model and the moments of the exact kinetic solution are shown. Figure 1a shows the evolution of the average particle

velocity. One can see that both variants of the PGM relax slightly too quickly to their steady-state values. The original log-normal PGM also under-estimates the average settling speed of the particles, however the deviation is not overly large. As predicted, the surface-weighted PGM predicts the steady settling velocity correctly.

In Figures 1b and 1c, the evolution of two components of the variance-covariance tensor are shown. One can see, in Figure 1b that the cloud of particles evolves from an initial vertical-velocity variance of $1\,\mathrm{m/s^2}$ to a higher value. Again, the new surface-weighted PGM settles to the correct value in the steady state. However, the deficiency of the original log-normal PGM is now much more clear. At steady-state the log-normal variant predicts a variance that is far to small. The effect of this will be that settling particles will not spread in space correctly.

Looking at Figure 1c, one can see a similar deficiency in the prediction by the log-normal PGM. Where the new surface-weighted PGM comes to the correct steady-state settling condition, the original log-normal variant under-predicts the final covariance. This covariance shows the dependency between a particle's size and its terminal velocity. It shows that larger particles will settle more quickly than smaller ones. As the original PGM underestimates this values, it will incorrectly predict the degree to which a cloud of settling particles will separate based on particle size.

The cause of the superiority of the new surface-weighted PGM for this case can be better understood by examining the evolution of the distribution function in each model. Figure 2 shows this evolution. In this figure, the two distribution functions are represented in a slice of phase space in the v_x-s plane. On the left, one observes the surface-weighted distribution as it relaxes towards the red line, which indicates the correct settling speed for particles of a given surface area. As time progresses, the distribution function eventually collapses onto the line.

On the right-hand side of Figure 2, the same settling for the log-normal distribution function is shown. The non-linear mapping between the space of the logarithm of particle diameter and particle surface area causes the distribution function to bend as it settles. In the end, the distribution function will never land on the correct line and will always under-predict relevant variances and covariances.

6.2 Three-Dimensional Sedimentation of a Puff of Particles

As a final demonstration case to show how the direct tracking of higher-order particle statistics yields information that is often invisible to traditional methods, a puff of particles with initial velocity moving and settling in a background cross wind is considered. The domain of this problem is a cube with five-meter sides. The puff is initially positioned at (x, y, z) coordinates of ($1\,\mathrm{m}$, $1\,\mathrm{m}$, $4\,\mathrm{m}$) and has a diameter of $0.5\,\mathrm{m}$. The particles for this case are assumed to follow a log-normal distribution of diameters. The original log-normal version of the PGM is considered first. Within the initial sphere of particles, the particle number density is $n = 29.6 \times 10^6\,\mathrm{particles/m^3}$. The mean surface area of the particles is $\sigma = 4.04 \times 10^{-6}\,\mathrm{m^2}$, with variance, Ψ_{ss} of $6.21 \times 10^{-12}\,\mathrm{m^4}$. The initial velocity is $3\,\mathrm{m/s}$ in the x direction with a variance of $0.1\,\mathrm{m/s^2}$ in all directions. All covariances are initially zero. The background wind is $1\,\mathrm{m/s}$ in the positive y direction. Particle properties are chosen such that the initial value of $\tau_{\mathcal{G}} = 0.1\,\mathrm{s}$. This allows all relevant physical processes to act on similar time scales. The initial condition is illustrated in Figure 3.

Calculations are done using a simple first-order finite-volume scheme using the HLL flux function [22]. A simple point-implicit time-marching scheme is used that treats the fluxes explicitly, while treating the local sources implicitly. This is necessary, as the source terms can often be stiff. Fortunately, as the sources take on simple expressions, this can be done quite easily. The domain is discretized using 4,096,000 cells, and time steps are limited by the maximum wave speed within the domain at every step with a CFL number of 0.15.

For this case, results are visualized at $t = 0.5\,\mathrm{s}$ and $t = 1\,\mathrm{s}$. Figure 4 shows the predicted average particle diameter at these two times. Regions where the number density of particles is larger than $1 \times 10^3\,\mathrm{particles/m^3}$ are visualized. One can clearly observe that the large particles have kept their initial velocity for longer, as they are less affected by particle drag. They have also been more heavily affected by gravity. This is why the larger particles have travelled farther in the x direction and fallen further. The smaller particles decelerated due to drag much more quickly and have a lower terminal velocity. They are also more strongly affected by the drag of the background wind. These effects cause a cloud of smaller particles to remain higher in the domain while translating more in the y direction due to the wind.

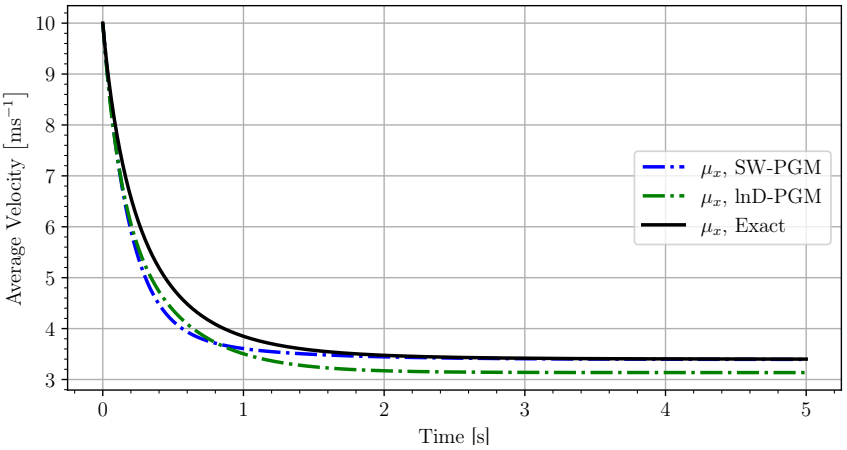

(a) Average velocity

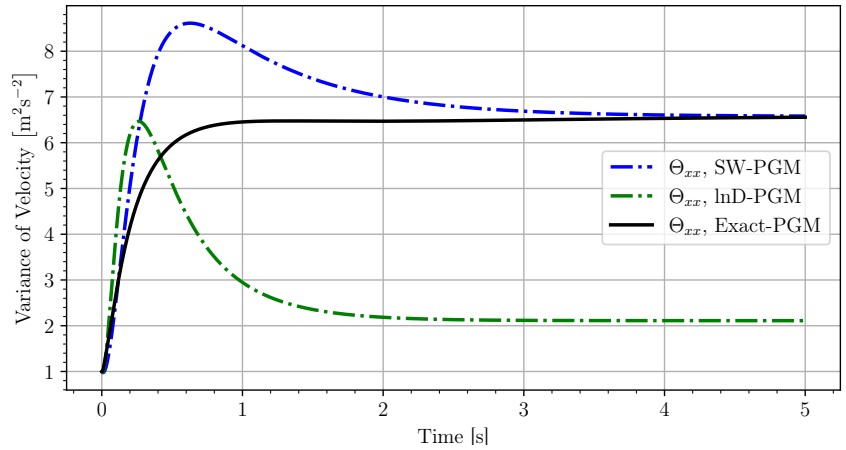

(b) Vertical velocity variance

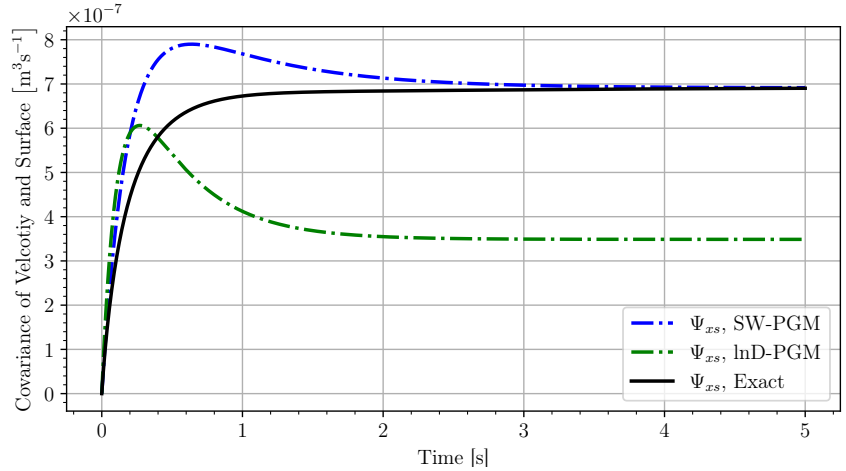

(c) vertical velocity-surface area covariance

Figure 1: Moment prediction for a settling cloud of particles subjected to gravity, buoyancy, and Stokes drag: exact kinetic solution, surface-weighted PGM and original log-normal PGM.

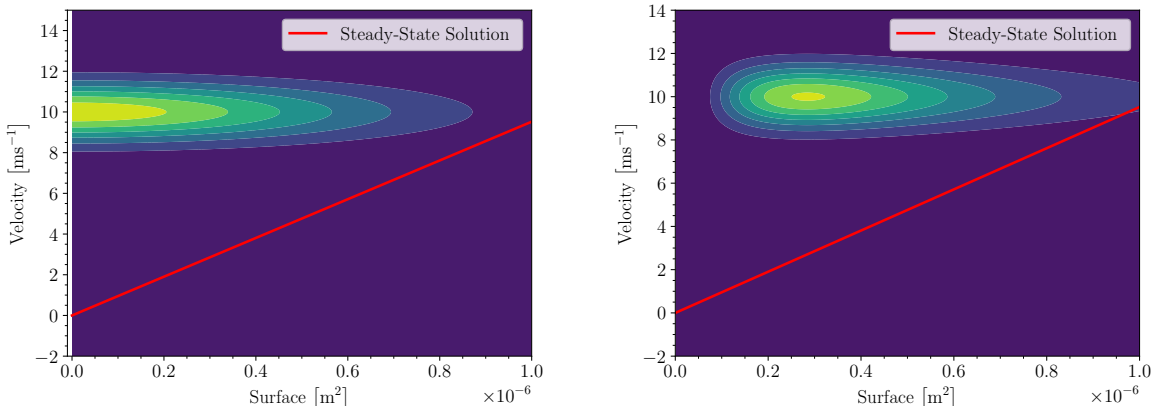

(a) SW-PGM, $t = 0\,\mathrm{s}$

(b) Log-normal PGM, $t = 0\,\mathrm{s}$

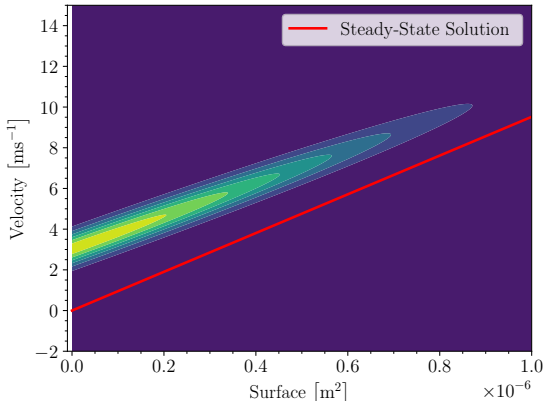

(c) SW-PGM, $t = 0.2\,\mathrm{s}$

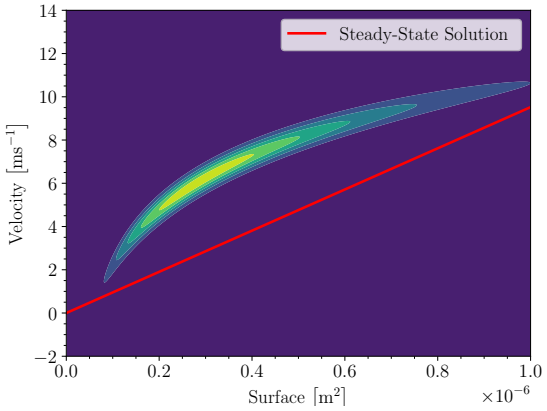

(d) Log-normal PGM, $t = 0.2\,\mathrm{s}$

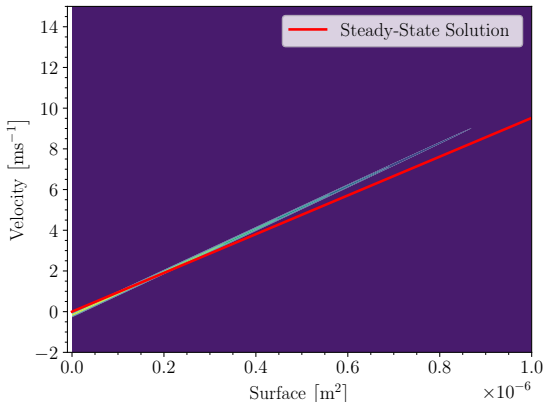

(e) SW-PGM, $t = 1.0\,\mathrm{s}$

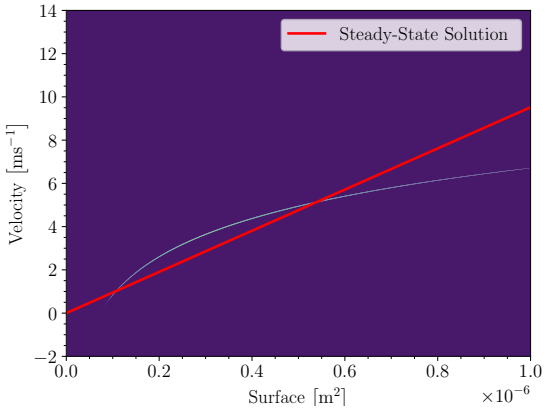

(f) Log-normal PGM, $t = 1.0\,\mathrm{s}$

Figure 2: Distribution function for a settling cloud of particles subjected to gravity, buoyancy, and Stokes drag as compared to the correct terminal velocity line: surface-weighted PGM and original log-normal PGM.

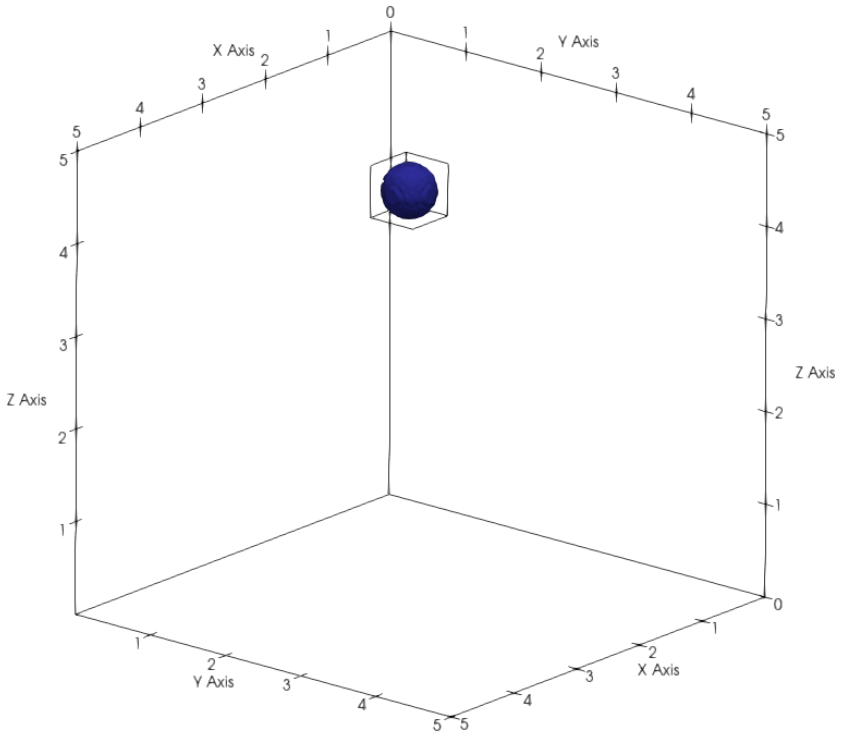

Figure 3: Initial condition for a puff of polydisperse particles with an initial x-direction bulk velocity with a cross wind in the y directions. Region where $n \geq 1 \times 10^3$ particles/m^3 is visualized.

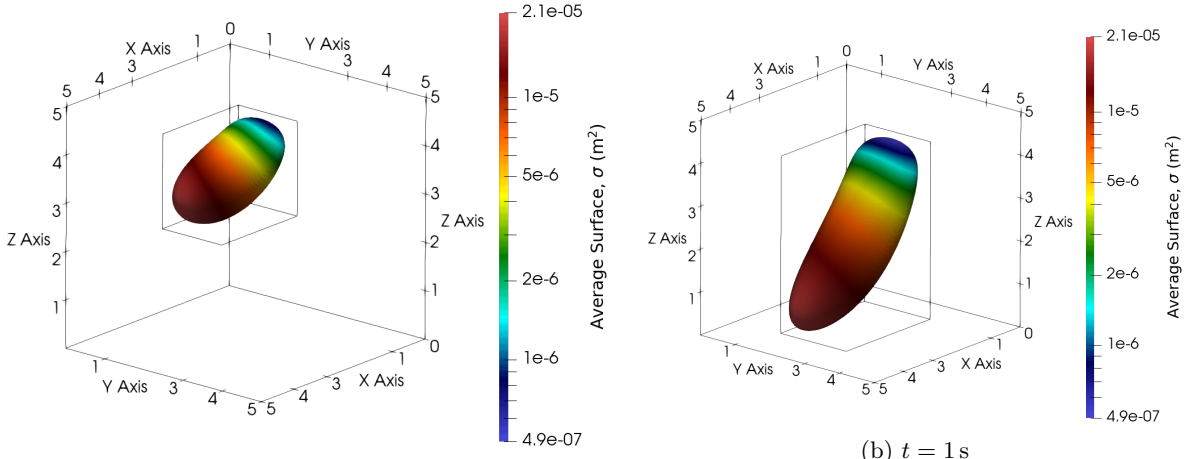

(a) $t = 0.5\,\mathrm{s}$

(b) $t = 1\,\mathrm{s}$

Figure 4: Particle size distribution. Region where $n \geq 1 \times 10^3$ particles/m^3 is visualized.

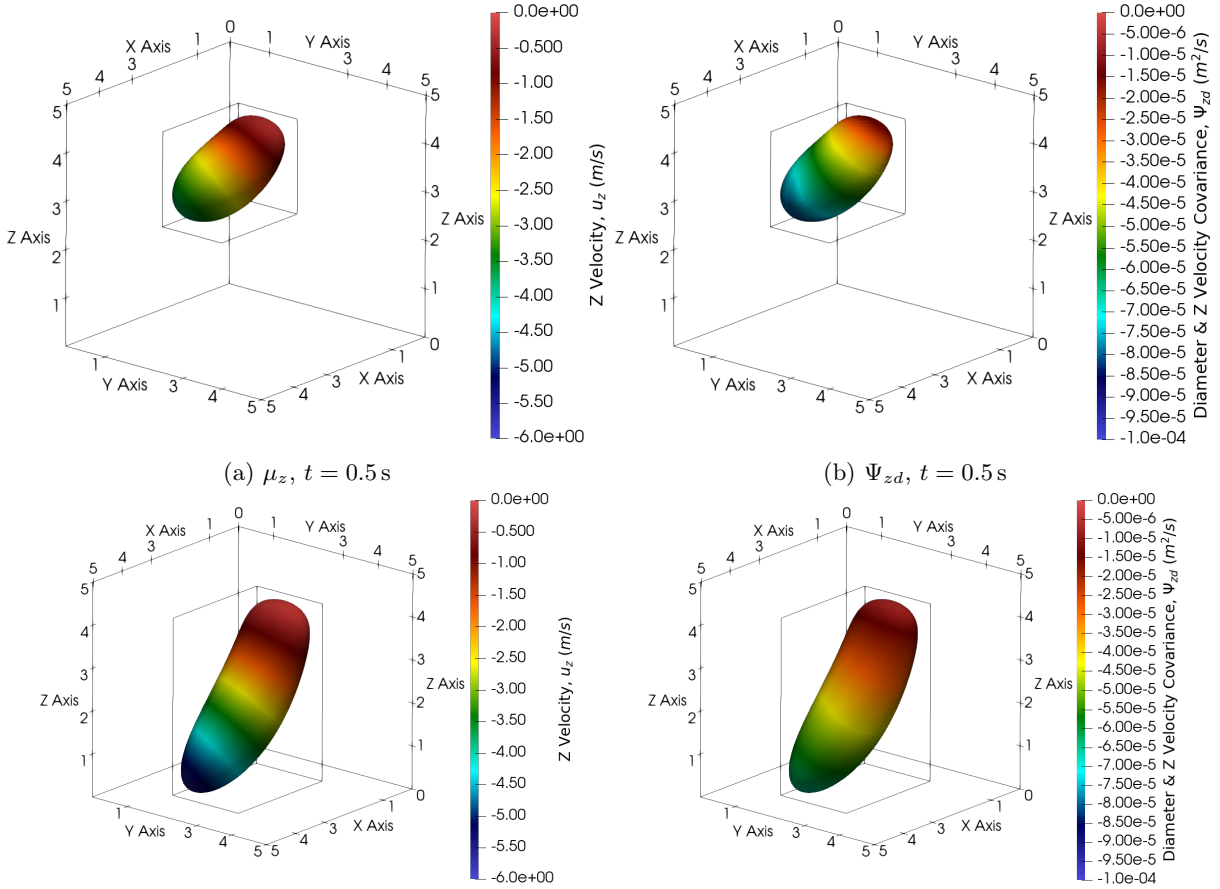

(a) μ_z, $t = 0.5\,\mathrm{s}$ (b) Ψ_{zd}, $t = 0.5\,\mathrm{s}$

(c) μ_z, $t = 1\,\mathrm{s}$ (d) Ψ_{zd}, $t = 1\,\mathrm{s}$

Figure 5: z-direction bulk velocity and covariance with particle size. Region where $n \geq 1 \times 10^3$ particles/m^3 is visualized.

The importance of the covariance between particle sizes and velocities is shown in Figures 5 and 6. Figure 5 examines the bulk vertical velocity and its covariance with particle size. In the left subfigures, one can clearly see that the particles that have fallen furthest have the most negative vertical velocity, obviously. More importantly, the right subfigures show that the covariance between the vertical component of the velocity and the particle size is always negative and has the highest magnitude in the particles that have fallen furthest. A negative covariance indicates that particles with largest negative vertical velocities are more likely to be larger particles. Again, this is entirely expected, however it is an effect that is not often directly considered by classical models. It is expected that this information will lead to improved predictive capabilities for the PGM models.

Figure 6 shows statistics related to the x-direction velocity. The left-hand subfigures show the x component of the bulk velocity. One can see that, at $t = 0.5\,\mathrm{s}$, the particles moving the fastest in this direction have a velocity of about $3\,\mathrm{m/s}$, which was the initial value. This is because there is a group of larger particles that has not yet been significantly slowed by drag and has travelled the largest distance in this direction. This is confined by examining the plots on the right, which show the covariance between the x component of velocity and the particle size. The positive value of this moment indicates that larger particles are more likely to have larger positive x-direction velocities. One can also observer that, by $t = 1\,\mathrm{s}$, drag forces have begun to have more of an effect on particles of all sizes. The average x-direction velocities are decreasing, as is the covariance.

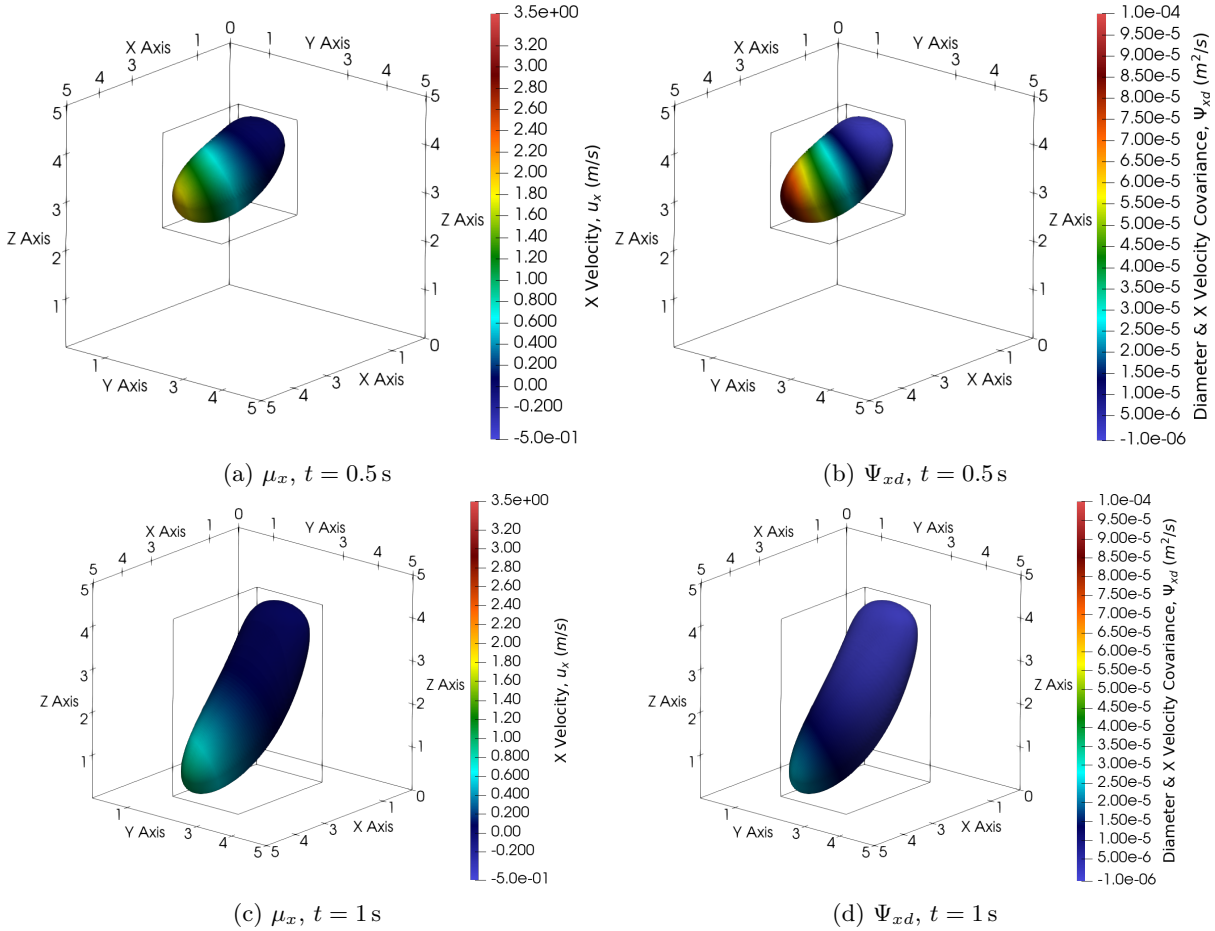

(a) μ_x, $t = 0.5\,\mathrm{s}$

(b) Ψ_{xd}, $t = 0.5\,\mathrm{s}$

(c) μ_x, $t = 1\,\mathrm{s}$

(d) Ψ_{xd}, $t = 1\,\mathrm{s}$

Figure 6: x-direction bulk velocity and covariance with particle size. Region where $n \geq 1 \times 10^3\,\mathrm{particles/m^3}$ is visualized.

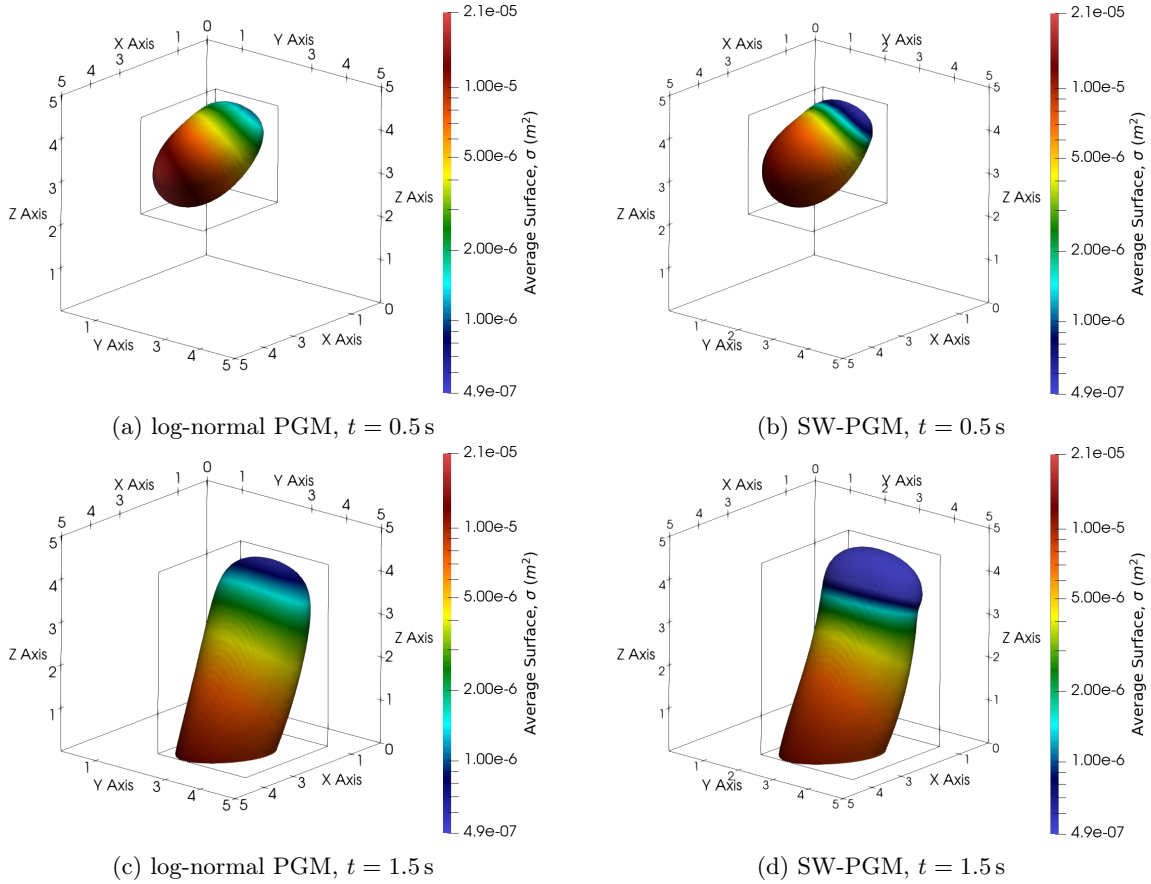

(a) log-normal PGM, $t = 0.5\,\mathrm{s}$

(b) SW-PGM, $t = 0.5\,\mathrm{s}$

(c) log-normal PGM, $t = 1.5\,\mathrm{s}$

(d) SW-PGM, $t = 1.5\,\mathrm{s}$

Figure 7: Particle size distribution as predicted by the log-normal and surface weighted versions of the PGM. Region where $n \geq 1 \times 10^3$ particles/m^3 is visualized.

6.2.1 Comparison with prediction of the surface-weighted PGM

As a final study, differences in the predicted solution for this problem provided by the original log-normal PGM and the new surface-weighted PGM are explored. Figure 7 compares the local particle-size distribution for this case as predicted by each model Results are visualized at $t = 0.5\,\mathrm{s}$ and $t = 1.5\,\mathrm{s}$. The left-hand subfigures were obtained from the log-normal PGM, which the right-hand figures used the surface-weighted PGM. For this case, differences are surprisingly minor. The exact shape of the region occupied by particles is slightly different and the distribution of particle sizes is not quite identical, however results are very close. The similarity of the two predictions is probably due to the fact that the variance in particle size is not overly large in this case. Though it is large enough to affect the flow, as demonstrated in the previous section. It is expected that larger differences in predictions should be expected for polydisperse flows that display a larger range of particle sizes.

7 Conclusion

This paper presented the derivation and analysis of two new models for the efficient prediction of polydisperse multiphase flows. These models belong to the family of Polydisperse Gaussian Models (PGM). In one model, the logarithm of the particle diameter is used to differentiate particle sizes, while, in the other, particle surface area is used. Regular and surface-weighted velocity moments are presented and used. Both models lead to first-order balance laws and are shown to be robustly hyperbolic. The surface-weighted version of the PGM is demonstrated to exactly recover the correct state for particles settling in a quiescent background. This is thought to be important for several practical problems. However, the surface-weighted version of the closure

brings added complexity and numerical difficulties that are not present in the original log-diameter version of the closure. The importance of high-order statistics of the particle phase to predictions are demonstrated for the three-dimensional case of a settling puff of particles in a cross wind.

Acknowledgements

This study was funded by the Natural Science and Engineering Research Council of Canada (NSERC) through grant number RGPIN-2020-06295 and by the Atomic Energy of Canada Limited, under the auspices of the Federal Nuclear Science and Technology Program. The research was conducted at the Canadian Nuclear Laboratories. Computational resources for this work were provided by the Argonne Leadership Computing Facility (ALCF) and the Niagara supercomputer at the SciNet HPC Consortium. The ALCF is a DOE Office of Science User Facility supported under Contract DE-AC02-06CH11357. The SciNet HPC consortium is funded by the Canada Foundation for Innovation; the Government of Ontario; Ontario Research Fund - Research Excellence; and the University of Toronto [23, 24]. The authors are very grateful for this support.

References

[1] R. Saurel, E. Daniel, and J. C. Loraud. Two-phase flows: Second-order schemes and boundary conditions. *AIAA J.*, 32(6):1214–1221, June 1994.

[2] S. A. Slater and J. B. Young. The calculation of inertial particle transport in dilute gas-particle flows. *Int. J. Multiphase Flow*, 27:61–87, 2001.

[3] A. Vié, F. Doisneau, and M. Massot. On the anisotropic Gaussian velocity closure for inertial-particle laden flows. *Commun. Comput. Phys.*, 17(1):1–46, 2015.

[4] F. Forgues and J. G. McDonald. Higher-order moment models for multiphase flows with accurate particle-stream crossing. *Int. J. Multiphase Flow*, 114:28–38, 2019.

[5] Daniele L. Marchisio, Jesse T. Pikturna, Rodney O. Fox, R. Dennis Vigil, and Antonello A. Barresi. Quadrature method of moments for population-balance equations. *AIChE Journal*, 49(5):1266–1276, 2003.

[6] R. O. Fox. A quadrature-based third-order moment method for dilute gas-particle flows. *J. Comput. Phys.*, 227:6313–6350, 2008.

[7] O. Desjardins, R. O. Fox, and P. Villedieu. A quadrature-based moment method for dilute fluid-particle flows. *J. Comput. Phys.*, 227:2514–2539, 2008.

[8] François Forgues, Lucian Ivan, Alexandre Trottier, and James G. McDonald. A gaussian moment method for polydisperse multiphase flow modelling. *Journal of Computational Physics*, 398, 12 2019.

[9] C David Levermore. Moment closure hierarchies for kinetic theories. *Journal of Statistical Physics*, 83, 1996.

[10] C. David Levermore and W. J. Morokoff. The Gaussian moment closure for gas dynamics. *SIAM J. Appl. Math.*, 59(1):72–96, 1998.

[11] Jinho Lee, Danbi Yoo, Seunghun Ryu, Seunghon Ham, Kiyoung Lee, Myoungsouk Yeo, Kyoungbok Min, and Chungsik Yoon. Quantity, size distribution, and characteristics of cough-generated aerosol produced by patients with an upper respiratory tract infection. *Aerosol and Air Quality Research*, 19(4):840–853, 2019.

[12] H. Grad. On the kinetic theory of rarefied gases. 2:331–407, 1949.

[13] T. I. Gombosi. *Gaskinetic Theory*. Cambridge University Press, Cambridge, 1994.

[14] W. Dreyer. Maximization of the entropy in non-equilibrium. *Journal of Physics A: Mathematical and General*, 20:6505–6517, 1987.

[15] I. Müller and T. Ruggeri. *Extended Thermodynamics*. Springer-Verlag, New York, 1993.

[16] S. L. Brown, P. L. Roe, and C. P. T. Groth. Numerical solution of a 10-moment model for nonequilibrium gasdynamics. Paper 95-1677, AIAA, June 1995.

[17] S. L. Brown. *Approximate Riemann Solvers for Moment Models of Dilute Gases*. PhD thesis, University of Michigan, 1996.

[18] J. G. McDonald. *Extended Fluid-Dynamic Modelling for Numerical Solution of Micro-Scale*. PhD thesis, University of Toronto, 2011.

[19] J. G. McDonald, J. S. Sachdev, and C. P. T. Groth. Application of Gaussian moment closure to micro-scale flows with moving and embedded boundaries. *AIAA J.*, 52:1839–1857, 2014.

[20] T. J. Barth. On discontinuous Galerkin approximations of boltzmann moment systems with Levermore closure. *Comp. Meth. Appl. Mech. Engrg.*, 195:3311–3330, 2006.

[21] Y. Suzuki and B. van Leer. Application of the 10-moment model to MEMS flows. Paper 2005-1398, AIAA, January 2005.

[22] A. Harten, P. D. Lax, and B. van Leer. On upstream differencing and Godunov-type schemes for hyperbolic conservation laws. *SIAM Rev.*, 25(1):35–61, 1983.

[23] M. Ponce, R. van Zon, S. Northrup, D. Gruner, J. Chen, F. Ertinaz, A. Fedoseev, L. Groer, F. Mao, B. C. Mundim, M. Nolta, J. Pinto, M. Saldarriaga, V. Slavnic, E. Spence, C.-H. Yu, and W. R. Peltier. Deploying a Top-100 supercomputer for large parallel workloads: the Niagara supercomputer. In *PEARC '19: Proceedings of the Practice and Experience in Advanced Research Computing on Rise of the Machines (learning)*, 2019.

[24] C. Loken, D. Gruner, L. Groer, R. Peltier, N. Bunn, M. Craig, T. Henriques, J. Dempsey, C.-H. Yu, J. Chen, L. J. Dursi, J. Chong, S. Northrup, J. Pinto, N. Knecht, and R. van Zon. SciNet: Lessons learned from building a power-efficient Top-20 system and data centre. In *J. Phys.: Conf. Ser.*, 2010.